Quaternary Layered Ni-Rich NCMA Cathode for Lithium-Ion Batteries

ABS. Li[$Ni_{1-x-y}Co_xAl_z$]O_2 (NCA) and Li[$Ni_{1-x-y}Co_xMn_y$]O_2 (NCM) cathodes have been the archetypes of current high-energy density cathodes for Li-ion batteries. A hybrid of NCA and NCM cathodes, a quaternary system consisting of Li[$Ni_{0.89}Co_{0.05}Mn_{0.05}Al_{0.01}$]$O_2$ (NCMA) was benchmarked against NCM and NCA with similar Ni contents. The quaternary NCMA cathode delivered a capacity of 228 mAh g^{-1} and outperformed the benchmarking cathodes in long-term cycling stability (85% after 1000 cycles). The reduction in the volume change during deintercalation and the enhanced intrinsic mechanical strength confirmed by the single particle compression test suppressed the microcrack nucleation and propagation. Microcrack suppression was important because microcracks serve as channels for electrolyte infiltration and lead to the subsequent surface degradation of internal surfaces. The proposed NCMA cathode provides extra cycling stability which is essential for electric vehicles, which require a long battery life and improvs the thermal stability of the cathode, which contributes to a safer battery.

With the rapid development of electric vehicles (EVs) and large-scale energy storage systems, the demand for high energy density rechargeable batteries has grown dramatically and the trend is expected to continue. Lithium-ion batteries (LIBs) have become the primary power source for EVs due to their high energy density, good rate capability, and long-term cycling performance. To satisfy the consumer-threshold driving range of 300 miles (480 km) per single charge,[1,2] extensive research for the development of high capacity cathodes has been carried out in the past decades.[3-10] Among the cathodes developed to date, a series of layered Ni-rich lithium transition metal oxides, $Li[Ni_{1-x-y}Co_xAl_z]O_2$ (NCA) or $Li[Ni_{1-x-y}Co_xMn_y]O_2$ (NCM), are the most promising candidates because they provide high reversible capacity with a long cycle life and high operating potential of 3.6 V vs. Li/Li^+. To further increase the capacity of current NCM and NCA cathodes, the fraction of Ni in the cathodes has been progressively increased;[11-13] however, this approach is limited by the deterioration of capacity retention and thermal stability resulting from excessive Ni enrichment (above x = 0.6 for NCM and 0.8 for NCA). One method for overcoming the obstacles posed by the Ni enrichment strategy is to dope alien metallic ions to pristine NCA or NCM cathodes to improve the structural stability and thus Li^+ intercalation stability.[14-25] Among the various doping metals, Al is the most widely used dopant because of its stabilizing role in the host layered structure. Moreover, it tends to improve the thermal stability owing to the stronger strength of Al-O bonds than those of Ni (Co, Mn)-O bonds.[14,20-22,24] However, the Al doping content should be carefully considered because of its non-participation in the redox reaction. Therefore, the Al fraction has been limited to a relatively low concentration below 5 mol%. Recently, we demonstrated that Al-doping greatly extends battery life as the 2 mol% Al-doped gradient $Li[Ni_{0.76}Co_{0.09}Mn_{0.15}]O_2$ cathode retained 95% of its initial capacity after 1000 cycles.[26]

Al-doping doping clearly improves the cycling stability of a Ni-rich NCM cathode (Figure S1) but accompanied by a concurrent capacity loss when introduced in excess. Here, we report a hybrid NCM and NCA cathode: $Li[Ni_{0.89}Co_{0.05}Mn_{0.05}Al_{0.01}]O_2$ (hereafter referred to as NCMA89) which provides an optimal combination of capacity and cycle life among cathodes with different Al content and whose performance surpasses that of the NCA and NCM cathodes with similar Ni contents. A comparative study of structural and electrochemical properties of $Li[Ni_{0.90}Co_{0.05}Mn_{0.05}]O_2$ (NCM90), $Li[Ni_{0.885}Co_{0.100}Al_{0.015}]O_2$ (NCA89), and NCMA89 is carried out by investigating bulk and surface structural degradation before and after long-term cycling.

Scanning electron microscopy (SEM) images of the NCA89, NCM90, and NCMA89 cathode particles show that the synthesized cathodes have spherical morphology with an average particle diameter of 10 μm (Figure S2a). There is no essential difference in the size and shape of particles among the three cathodes, implying that particle morphology is an unlikely factor affecting the electrochemical performance of the cathodes. X-ray diffraction (XRD) patterns of the NCA89, NCM90, and NCMA89 cathodes in Figure S2b are indexed to a α-$NaFeO_2$ structure with $R\bar{3}m$ space group, and no impurity phases were observed. Both *a*- and *c*-axis parameters for the tested cathodes in Table S1 were similar in magnitude.

Figure 1a shows the initial charge-discharge curves of the three cathodes cycled between 2.7 and 4.3 V at 0.1 C (18 mA g^{-1}) at 30 °C in 2032 coin-type half-cells. NCM90 delivers a high initial discharge capacity of 229 mAh g^{-1}. In comparison, the NCMA89 cathode exhibits a slightly reduced capacity of 228 mAh g^{-1} due to the addition of inactive Al, while the NCA89 cathode produces a yet lower capacity of 225 mAh g^{-1}. Interestingly, the NCMA89 cathode, as shown in Figure 1b, exhibits a substantial improvement in capacity retention at 90.6% after 100 cycles compared to the NCA and NCM cathodes although the Al doping level was limited to a mere 1 mol%. The NCM90 and NCA89 cathodes exhibit a capacity retention of 87.7% and 83.7%, respectively, during the same cycling period. Increasing the upper cutoff voltage to 4.5 V further substantiates enhancement of the cycling stability by the addition of Al to NCM90, as NCMA89, NCM90, and NCA89 maintain 87.1, 82.3, and 73.3% of their respective initial capacities after 100 cycles at 0.5 C (Figure 1c). Moreover, the NCM90 cathode apparently exhibits better Li intercalation stability than the NCA89 cathode when charged to 4.3 V and 4.5 V. The improved cycling stability is emphasized during long-term cycling of the cathodes in aluminum pouch-type full cells using a graphite anode. As shown in Figure 1d, the full cell with the NCMA89 cathode exhibits outstanding capacity retention of 84.5 % after 1000 cycles, while NCM90 and NCA89 cathodes retain only 60.2% and 57.9% of their respective initial capacities, respectively. The cycling stability of the NCMA89 cathode at an elevated temperature (45 °C) is much better than that of the NCM90 and NCA89 cathodes (Figure 1e). After 500 cycles, 82.6% of the initial capacity of NCMA89 is retained, while that of the NCM90 and NCA89 cathodes is limited 53.8% and 50.0% respectively.

To study the effect of the H2↔H3 phase transition, $dQ\ dV^{-1}$ profiles were obtained by numerically differentiating the charge-discharging curves (Figure S3a, S3b). All the three Ni-rich cathodes undergo multiphase transitions during Li^+ removal and insertion. The intensity changes of the redox peaks at ~4.2 V corresponding to the H2↔ H3 phase transition during cycling correlates well with the relative cycling stability of the three cathodes. For both NCA89 and NCM90 cathodes, the deteriorating reversibility of the redox peak is clearly observed as the H2↔H3 peak intensity gradually decreases during cycling, whereas that of the NCMA89 cathode remains nearly unchanged during the same cycling period. The relative reversibility of the H2→H3 phase transition can be better seen in Figure S3c, S3d, which illustrates the normalized integrated peak intensity against the cycle number. The superior structural stability of the NCMA89 cathode is pronouncedly advertised when cycled at 4.5 V, as the H2→H3 peak for NCA89 and NCM90 cathodes decay at a much faster rate in comparison to the NCMA89 cathode (Figure S2b, S2d). To explicitly demonstrate the deleterious effect of the H2→H3 phase transition, which causes highly anisotropic strain in the deeply charged state, a series of *in situ*

XRD experiments were performed while charging the three cathodes from 3.3 to 4.5 V at a constant current density of 36 mA g^{-1}. The lattice parameters estimated from the XRD data are plotted as a function of the state of charge in **Figures 2a** and S3. As equal amounts of Li ions are extracted from each cathode, the *a*-axis parameter continuously decreases. The magnitude of the overall lattice parameter reduction, Δa is 2.1 – 2.2% for the three cathodes (Figure S3). However, in the *c*-direction, the lattice parameter gradually increases and then contracts sharply at the onset of the H2 → H3 phase transition. This abrupt contraction in the *c*-direction, which amounts to ~ 4%, undermines the mechanical integrity of the secondary particle. The mechanical strain triggered by this phase transition is further aggravated by its anisotropy, since the contraction in the *a*-direction is limited to ~0.5% while the unit cell concurrently contracts by 4 % in the *c*-direction during the phase transition. Hence, the extent of the *c*-axis contraction during the H2 → H3 phase transition critically determines the magnitude and the distribution of the local internal strain. Δc for the NCMA89 cathode was considerably lower than that of the NCA89 and NCM90 cathodes (Figure 2a). The effect of the reduced strain for the NCMA89 cathode is manifested by reduced or lack of microcracks in the secondary particles of the NCMA89 cathode in its deeply charged state ($x = 0.85$) whereas visible microcracks were observed in the cross-sectional images even in the first charge state for the other two cathodes (Figure 2b-d). In the case of the NCA89 cathode, the microcracks that nearly fractured the secondary particles were observed at $x = 0.85$, which is in agreement with the noticeably faster capacity fading observed when the cathode cycles at 4.5 V (Figure 2b). The cross-sectional images of the both 1000 cycled NCA89 and NCM90 cathode particles fractured along the interparticle boundaries, almost pulverizing the cathode particles (Figure 2e,f) whereas the NCMA89 secondary particles remained mostly free of any microcracks (in the discharged state) even after performing 1000 cycles (Figure 2g) Images of the cycled electrodes suggest that the introduction of a minute amount of Al not only reduces the magnitude of the anisotropic strain in the deeply charge state but also appears to increase the interparticle boundary strength, which is plausible since Al-O bonds provide strong bonding.[13,25,27,28] To directly verify the enhancement of the fracture toughness by Al-doping, the fracture strength of a single particle from each cathode was measured using a micro-compression tester. As expected, shown in Figure S4, the NCMA89 particle withstood a force of 22.9 mN which amounts to a particle strength of 185.7 MPa. In comparison, the failure load of the NCA89 particle was limited to only 12.9 mN force (particle strength of 125.5 MPa), while the NCM90 particle had a slightly larger particle strength (force of 14.0 mN and particle strength of 137.2 MPa) than that of NCA89. The particle strength data correlate well with the long-term cycling behavior of the three cathodes and the Al-doping toughens the boundaries among primary particles to retard microcrack formation during the deleterious phase transition.[29,30]

The mechanical stability imparted by Al-doping for the NCMA89 cathode (i.e. retardation of the microcrack nucleation and propagation) brings an additional benefit because the microcracks serve as channels for the electrolyte infiltration into the particle interior. The infiltrated electrolyte attacks the internal exposed surface and increases the cathode’s impedance through the continuous accumulation of a passivating NiO-like impurity layer on the particle surfaces.[31.32] Electrochemical impedance spectroscopy (EIS) was used to measure the impedance at the charged state. The impedance growth anticipated from the cycling data was clearly observed for the three cathodes (Figure S5a-c). The three cathodes exhibit a similar surface film resistance, which hardly changes during the entire cycling duration. Meanwhile the R_{ct} of the NCA89 cathode increases from 6.3 Ω to 55 Ω after 100 cycles whereas the NCMA89 cathode has a relatively stable R_{ct} value at 33 Ω after same cycling period (Figure S5d). The R_{ct} values from EIS data verify that the electrolyte infiltration into the particle interior is substantially reduced in the NCMA89 cathode, since the three cathodes have a similar particle diameter and the damage of the external particle surface is likely identical in extent for the three cathodes. The relative electrolyte damage was also confirmed using TEM analysis of the cycled cathodes. The dark-field STEM image of the cycled NCA89 cathode shows a major crack traversing the entire particle and nearly fracturing the secondary particle into two halves (**Figure 3a**). Although several cracks in the cycled NCM90 cathode reached the particle surface and expedited the electrolyte infiltration (Figure 3b), the secondary particle remained mechanically intact. In turn, no visible cracks were observed in the NCMA89 cathode, attesting to its superior mechanical stability (Figure 3c). While assessing the surface structure degradation using high-resolution TEM (HR-TEM), a typical NiO-like surface layer that increases the charge transfer resistance was observed on the surface of the cycled NCA89 cathode, as shown in Figure 3d. Local Fourier transforms images of the cycled cathode show that the surface rocksalt layer was confined to a thickness of ~10 nm. Figure 3e shows the surface damaged layer of the cycled NCMA89 cathode whose thickness was 5–7 nm, demonstrating the extent of the impedance-increasing surface damage was roughly the same for the three cathodes. However, the HR-TEM image of an interior grain along the microcrack in the NCA89 cathode in Figure 3f reveals that the rocksalt layer was substantially thicker (~ 40 nm) compared to that found on the surface grain (5–10 nm). It appears that the exposed interior surfaces on the interior primary particles are relatively more susceptible to the electrolyte attack. Once the microcracks originating the particle core extend to the external surface during charging (Li removal phase) and thereby allow electrolyte infiltration, crack faces are exposed to electrolyte attack. These internal surfaces are more vulnerable to electrolyte attack compared to the external surfaces, as Li migration out of the particle core likely leaves the particle interior in a Li-deficient state, which is thermodynamically unstable and predisposed to the phase transformation to the rocksalt state. The TEM analysis in agreement with the EIS result, i.e. the R_{ct} build-up observed in the NCA89 cathode mostly stems from the degradation of the interior surface exposed to the electrolyte through the microcracks. Thus, the retardation of the microcrack formation in the NCMA89 cathode not only reinforces the mechanical integrity of the secondary particles in the Ni-rich layered cathodes as well as the chemical stability against the electrolyte attack by preventing infiltration of the electrolyte into the particle interior.

Recently, it was proposed that the oxygen release from the lattice during deintercalation promotes the transition metal dissolution and destabilizes the crystal structure of the layered cathodes.[33,34] Density functional calculation is employed to calculate the lithium and oxygen vacancy energies of the three cathodes in order to elucidate the Al-doping effect on the intrinsic structural stability of the three cathodes. To compute the average values of Li vacancy formation energies ($\acute{E}_V^{Li}$), we have considered fully lithiated NCA89, NCM90, and

NCMA89. Li vacancy energies of the cathodes are calculated for 16 different vacancy sites (Alphabet marking) shown in Figure S6 and Table S2. The respective average Li vacancy energies for the NCA89, NCM90, and NCMA89 is 3.96 eV, 3.94 eV, and 3.97 eV. These nearly identical Li vacancy energies suggest that the energy required for Li intercalation/deintercalation for the three cathodes is nearly equal for the three cathodes because of their similar compositions, which is in agreement with the fact that the initial discharge capacities delivered by the three cathodes were almost same. The O vancancy formation energies ($\acute{E}_V^O$), are also nearly identical for the three cathodes (**Figure 4**). The difference in the structural stability is, however, clearly observed in the O vacancy energy calculated with 89 % of Li atoms removed from each lattice. The respective O vacancy energies for the three cathodes in the delithiated state are calculated for 37 different O sites as shown in Figure 4 and the O vacancy energies are also listed in the accompanying tables. The average O vacancy energies are 0.87 eV, 0.72 eV, and 0.80 eV for the NCA89, NCM90, and NCMA89, respectively, indicating that the oxygen atoms are least likely released from the NCA89 cathode as conjectured from the strong binding energy of Al-O bonds. The density functional calculation provides a strong basis for confirming the relative high structural stability of the NCA89 cathodes, in general, compared to the NCM90 cathodes. Incidentally, the O vacancy energy for the NCMA89 cathode is an average of the vacancy energies of the NCA89 and NCM90 cathodes so that the NCMA89 cathode partially benefits from the improved structural stability in the delithiated state by having Al ions in its lattice.

To further support the relative structural stability of NCA89, NCM90, and NCMA89 cathodes that has been established thus far, the electrochemically delithiated cathodes ($Li_{0.3}MO_2$, M = Ni, Co, Mn, and/or Al) were characterized by in situ time-resolved XRD (TR-XRD) in Ar-atmosphere (**Figure 5a-c**). The delithiated NCMA89 retained its $R\bar{3}m$

structure up to 170 °C after which a cubic spinel structure ($Fd\bar{3}m$) was detected. The disordered spinel phase gradually changed to rocksalt structure ($Fm\bar{3}m$) starting at 190 °C. At 370 °C, the NCMA89 completely transformed to the rocksalt structure. In contrast, the disordered spinel structure was observed starting at 180 °C for NCA89 cathode and 160 °C for the NCM90 cathode, and a complete transformation to the rocksalt structure for the two cathodes occurred at 340 °C. Thermal stability of cathode is also important characteristics to the battery safety. As see Differential scanning calorimetry (DSC) data in Figure 5d, the onset temperature of the exothermic reaction for the NCA89 was 200 °C with peak generation of 1,753 J g^{-1} while NCM90 exhibited onset temperature of 190 °C and heat generation of 1,561 J g^{-1}. In comparison, NCMA89 demonstrates improved thermal stability with exothermic peak temperature of 205.4 °C and reduced heat generation of 1,384 J g^{-1}. It is believed that the improved thermal property of NCMA89 is ascribed to the decreased amount of microcracks which contains less amount of electrolyte. These results clearly demonstrate that the NCMA89 is structurally stable due to a synergetic effect of Al and Mn ions stabilizing the layered structure and delaying the thermally induced phase transitions.

We have demonstrated that a hybrid of Ni-rich NCA and NCM cathodes, a quaternary system consisting of $Li[Ni_{0.89}Co_{0.05}Mn_{0.05}Al_{0.01}]O_2$ is capable of outperforming both NCA89 and NCM90 with similar Ni contents in terms of cycling and thermal stabilities. The *insitu* XRD analysis shows that the Al-doping effect is rather subtle, as the volume contraction/expansion during the H2 ↔ H3 phase transition is slightly reduced by the Al-doping of the NCM cathode. This reduction in volume change, however, together with the enhanced intrinsic mechanical strength directly confirmed by the single particle compression test, is sufficient to suppress microcrack nucleation and propagation. It was shown that the microcrack suppression observed in the NCMA89 cathode was the key in ensuring its long-term cycling stability as microcracks serve as channels for the electrolyte infiltration and lead to the subsequent surface degradation of internal surfaces. The proposed Ni-enriched NCMA cathode provides extra cycling stability which is essential in the case of EVs which require a long battery life (> 500 cycles). The structural stability gained by the Al-doping also improved the thermal stability of the cathode, which contributes to a safer battery.

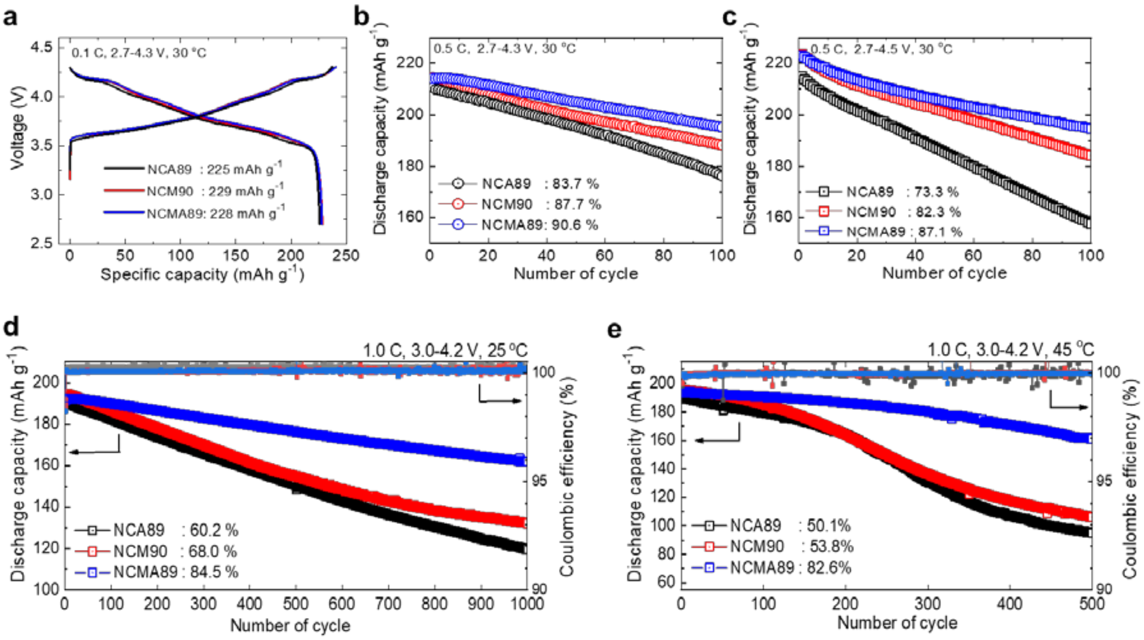

Figure 1. Electrochemical performance of the NCA89, NCM90 and NCMA89. (a) 1st cycle voltage profiles for three cathodes. All cells are operated within a voltage range of 2.7–4.3 V at 0.1 C and 30 °C in a half cell using Li metal as an anode. Cycling performance of the three cathodes tested within a voltage range of (b) 2.7–4.3 V and (c) 2.7–4.5 V at 0.5 C. Long term cycling of NCA89, NCM90 and NCMA89 cathodes, tested using pouch full cells at 1.0 C, (d) 25 °C and (e) 45 °C within a voltage range of 3.0–4.2 V with natural graphite as an anode.

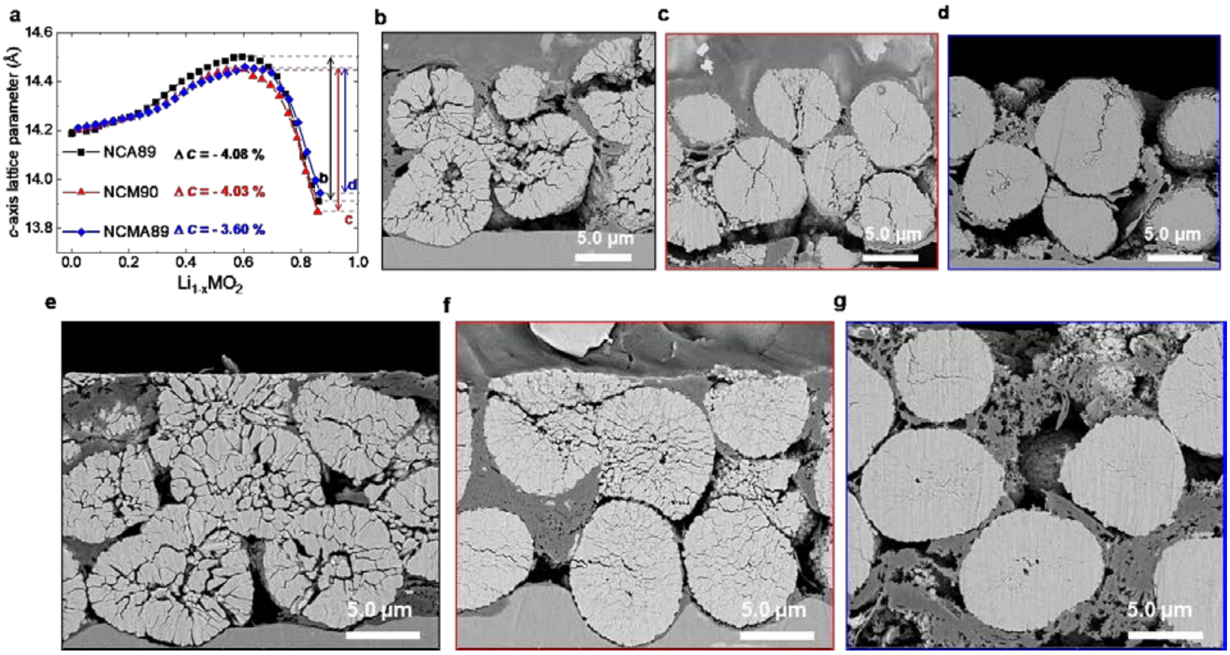

Figure 2. (a) *c*-axis lattice parameters of NCA89, NCM90 and NCMA89 as a function of the amount of lithium in the cathode. Cross-sectional SEM images as a function of the amount of lithium in the cathode. $Li_{1-x}MO_2$ x=0.85: (b) NCA89, (c) NCM90, and (d) NCMA89. Cross-sectional SEM images of discharge-state after 1000 cycles; (e) NCA89, (f) NCM90, and (g) NCMA89.

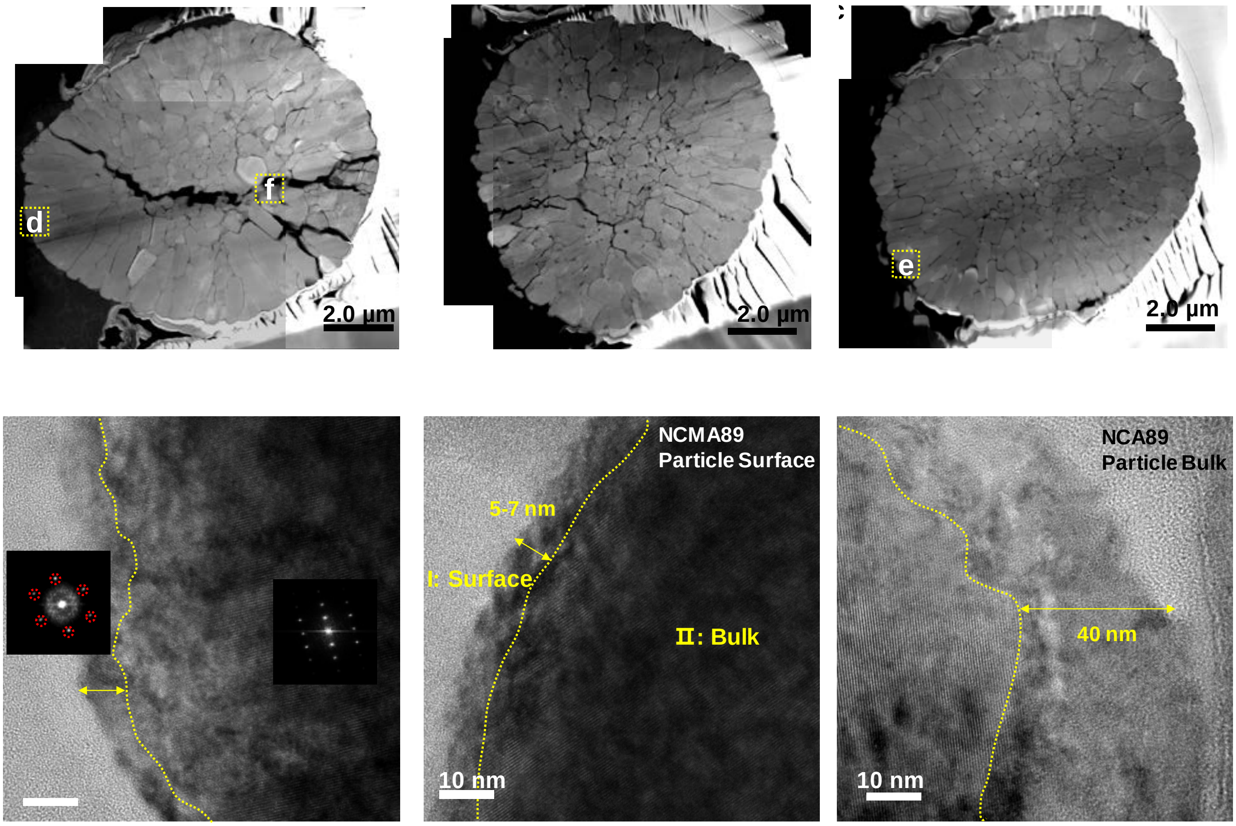

Figure 3. Mosaic scanning TEM images of cycled electrodes after 100 cycles using the half cell: (a) NCA89, (b) NCM90, and (c) NCMA89. High-magnification TEM images of the Particle surface (d) NCA89 and (e) NCMA89 cathode after 100 cycles: High-magnification TEM images correspond to the region marked by the yellow box in (a,c). Fourier filtered transforms of the marked regions by numerals in (d). (f) The TEM image of the particle bulk NCA89 cathode after 100 cycles: High-magnification TEM images of the region marked by the yellow box in (a).

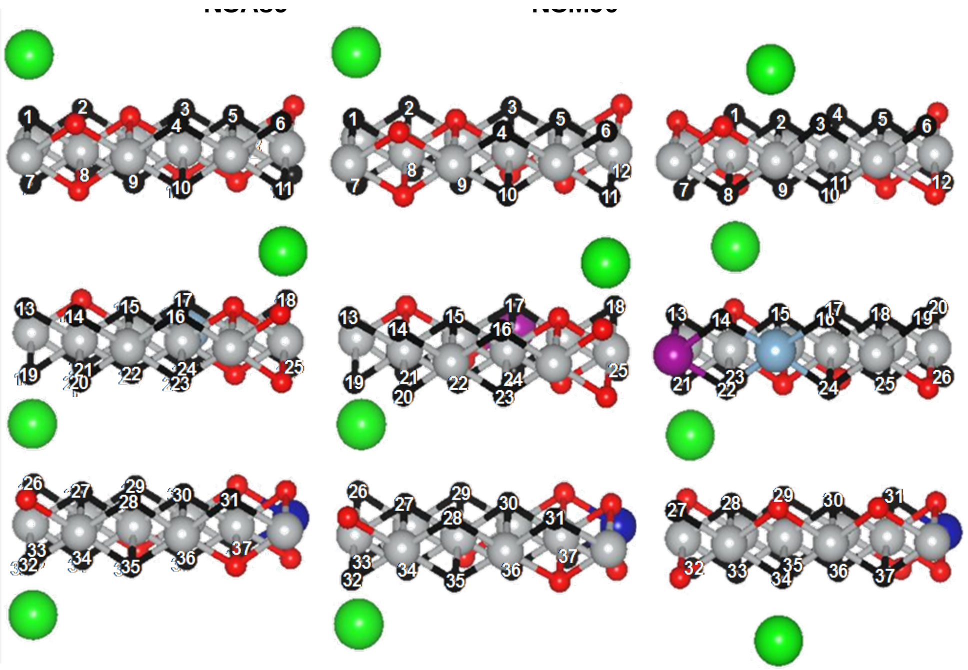

NCA89	E_V^0(eV)		E_V^0(eV)		E_V^0(eV)
1	1.20	14	0.67	27	0.51
2	1.19	15	0.97	28	1.21
3	0.81	16	0.96	29	0.67
4	0.67	17	0.77	30	0.33
5	0.76	18	0.96	31	0.85
6	0.64	19	1.02	32	0.31
7	0.64	20	0.88	33	1.26
8	1.17	21	1.10	34	0.88
9	0.74	22	0.74	35	0.56
10	1.02	23	1.10	36	0.58
11	1.19	24	0.77	37	1.10
12	0.62	25	1.40		
13	0.94	26	1.05		

$$\bar{E}_V^0(\mathrm{eV}) = 0.87\ \mathrm{eV}$$

NCM90	E_V^0(eV)		E_V^0(eV)		E_V^0(eV)
1	1.19	14	1.15	27	0.34
2	1.19	15	0.47	28	1.13
3	0.59	16	0.66	29	0.46
4	0.71	17	0.09	30	0.14
5	0.70	18	0.64	31	0.69
6	0.61	19	0.59	32	0.16
7	0.61	20	1.14	33	0.98
8	1.08	21	0.75	34	0.73
9	0.71	22	0.13	35	0.38
10	0.95	23	0.77	36	0.41
11	1.15	24	1.20	37	0.81
12	0.60	25	0.50		
13	1.36	26	1.01		

$$\bar{E}_V^0(\mathrm{eV}) = 0.72\ \mathrm{eV}$$

NCMA89	E_V^0(eV)		E_V^0(eV)		E_V^0(eV)
1	0.59	14	1.57	27	0.25
2	0.58	15	0.79	28	0.33
3	0.75	16	1.20	29	0.11
4	0.56	17	0.67	30	0.44
5	0.11	18	0.89	31	2.04
6	0.48	19	1.34	32	0.91
7	0.76	20	0.92	33	0.34
8	0.57	21	0.85	34	1.80
9	0.77	22	1.17	35	0.29
10	0.48	23	1.08	36	1.54
11	0.58	24	0.86	37	0.41
12	0.61	25	0.93		
13	1.08	26	0.83		

$$\bar{E}_V^0(\mathrm{eV}) = 0.80\ \mathrm{eV}$$

Figure 4. Side views of atomic structures and Calculated E_V^O and $\acute{E}_V^O$ values of NCA89, NCM90, and NCMA89 with 89% removed Li ions showing different O vacancy sites for which we calculated formation energy.

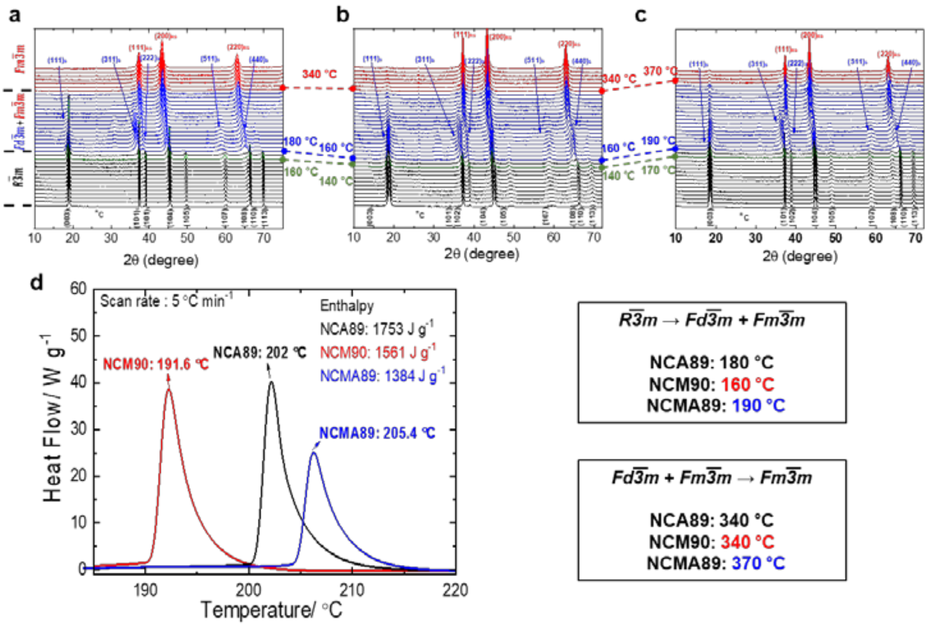

Figure 5. Time-resolved XRD patterns for (a) NCA89, (b) NCM90, and (c) NCMA89; heated in the temperature range from 25 to 450 °C in the Argon atmosphere. (d) DSC profiles for the NCA89, NCM90, and NCMA89 cathodes.

REFERENCES

(1) U.S. Department of Energy. Annual Merit Review - Energy Storage Technologies. https://www.energy.gov/eere/vehicles/annual-merit-review-presentations (2012).

(2) Myung, S.-T.; Maglia, F.; Park, K.-J.; Yoon, C. S.; Lamp, P.; Kim, S.-J.; Sun, Y.-K. Nickel-Rich Layered Cathode Materials for Automotive Lithium-Ion Batteries: Achievements and Perspectives. *ACS Energy Lett.* **2017**, *2*, 196-223.

(3) Saadoune, I.; Delmas, C. $LiNi_{1-y}Co_yO_2$ Positive Electrode Materials: Relationships between the Structure, Physical Properties and Electrochemical Behavior. *J. Mater. Chem.* **1996**, *6*, 193-199.

(4) Liu, Z.; Yu A.; Lee, J. Y. Synthesis and Characterization of $LiNi_{1-x-y}Co_xMn_yO_2$ as the Cathode Materials of Secondary Lithium Batteries. *J. Power Sources* **1999**, *81-82*, 416-419.

(5) Ohzuku, T.; Makimura, Y. Layered Lithium Insertion Material of $LiNi_{1/2}Mn_{1/2}O_2$: A Possible Alternative to $LiCoO_2$ for Advanced Lithium-Ion Batteries. *Chem. Lett.* **2001**, *30*, 744-745.

(6) Kostecki, R.; McLarnon, F. Local-Probe Studies of Degradation of Composite $LiNi_{0.8}Co_{0.15}Al_{0.05}O_2$ Cathodes in High-Power Lithium-Ion Cells. *Electrochem. Solid State Lett.* **2004**, *7*, A380-A383.

(7) Kondo, H.; Takeuchi, Y.; Sasaki, T.; Kawauchi, S.; Itou, Y.; Hiruta, O.; Okuda, C.; Yonemura, M.; Kamiyama, T.; Ukyo, Y. Effects of Mg-Substitution in $Li(Ni,Co,Al)O_2$ Positive Electrode Materials on the Crystal Structure and Battery Performance. *J. Power Sources* **2007**, *174*, 1131-1136.

(8) Sun, Y.-K.; Myung, S.-T.; Park, B.-C.; Prakash, J.; Belharouak, I.; Amine, K. High-Energy Cathode Material for Long-Life and Safe Lithium Batteries. *Nat. Mater.* **2009**, *8*, 320-324.

(9) Zhou, P.; Meng, H.; Zhang, Z.; Chen, C.; Lu, Y.; Cao, J.; Cheng, F.; Chen, J. Stable Layered Ni-rich $LiNi_{0.9}Co_{0.07}Al_{0.03}O_2$ Microspheres Assembled with Nanoparticles as High-Performance Cathode Materials for Lithium-Ion Batteries. *J. Mater. Chem. A* **2017**, *5*, 2724-2731.

(10) Kim, U.-H.; Jun, D.-W.; Park, K.-J.; Zhang, Q.; Kaghazchi, P.; Aurbach, D.; Major, D. T.; Goobes, G.; Dixit, M.; Leifer, N.; Wang, C.; Yan, P.; Ahn, D.; Kim,

K.-H.; Yoon, C. S.; Sun, Y.-K. Pushing the Limit of Layered Transition Metal Oxide Cathodes for High-Energy Density Rechargeable Li Ion Batteries. *Energy Environ. Sci.* **2018**, *11*, 1271-1279.

(11) Noh, H.-J.; Youn, S.; Yoon, C. S.; Sun, Y.-K. Comparison of the Structural and Electrochemical Properties of Layered Li[$Ni_xCo_yMn_z$]O_2 (x = 1/3, 0.5, 0.6, 0.7, 0.8 and 0.85) Cathode Material for Lithium-Ion Batteries. *J. Power Sources* **2013**, *233*, 121-130.

(12) Sun, H.-H.; Choi, W.; Lee, J. K.; Oh, I.-H.; Jung, H.-G. Control of Electrochemical Properties of Nickel-Rich Layered Cathode Materials for Lithium Ion Batteries by Variation of the Manganese to Cobalt Ratio. *J. Power Sources* **2015**, *275*, 877-883.

(13) Yoon, C. S.; Choi, M. H.; Lim, B.-B.; Lee, E.-J.; Sun, Y.-K. Review—High-Capacity Li[$Ni_{1-x}Co_{x/2}Mn_{x/2}$]O_2 (x = 0.1, 0.05, 0) Cathodes for Next-Generation Li-Ion Battery. *J. Electrochem. Soc.* **2015**, *162*, A2483-A2489.

(14) Lim, J.-M.; Hwang, T.; Kim, D.; Park, M.-S.; Cho, K.; Cho, M. Intrinsic Origins of Crack Generation in Ni-rich $LiNi_{0.8}Co_{0.1}Mn_{0.1}O_2$ Layered Oxide Cathode Material. *Sci. Rep.* **2017**, *7*, 39669.

(15) Kondrakov, A. O.; Schmidt, A.; Xu, J.; Geßwein, H.; Mönig, R.; Hartmann, P.; Sommer, H.; Brezesinski, T.; Janek, J. Anisotropic Lattice Strain and Mechanical Degradation of High- and Low-Nickel NCM Cathode Materials for Li-Ion Batteries. *J. Phys. Chem. C* **2017**, *121*, 3286-3294.

(16) Chowdari, B.V.R.; Subba Rao G.V.; Chow, S.Y. Cathodic Behavior of (Co, Ti, Mg)-Doped $LiNiO_2$. *Solid State Ionics* **2001**, *140*, 55-62.

(17) Subramanian, V.; Fey, G. T.-K. Preparation and Characterization of $LiNi_{0.7}Co_{0.2}Ti_{0.05}M_{0.05}O_2$ (M=Mg, Al and Zn) Systems as Cathode Materials for Lithium Batteries. *Solid State Ionics* **2002**, *148*, 351-358.

(18) Croguennec, L.; Suard, E.; Willmann P.; Delmas C. Structural and Electrochemical Characterization of the $LiNi_{1-y}Ti_yO_2$ Electrode Materials Obtained by Direct Solid-State Reactions. *Chem. Mater.* **2002**, *14*, 2149-2157.

(19) Kondo, H.; Takeuchi, Y.; Sasaki, T.; Kawauchi, S.; Itou, Y.; Hiruta, O.; Okuda, C.; Yonemura, M.; Kamiyama, T.; Ukyo, Y. Effects of Mg-substitution in $Li(Ni,Co,Al)O_2$ Positive Electrode Materials on the Crystal Structure and Battery Performance. *J. Power Sources* **2007**, *174*, 1131-1136.

(20) Zhou, F.; Zhao, X.; Lu, Z.; Jiang, J.; Dahn, J.R. The Effect of Al Substitution on the Reactivity of Delithiated $LiNi_{1/3}Mn_{1/3}Co_{(1/3-z)}Al_zO_2$ with Non-Aqueous Electrolyte. *Electrochem. Commun.* **2008**, *10*, 1168-1171.

(21) Woo, S.-W.; Myung, S.-T.; Bang, H.; Kim, D.-W.; Sun, Y.-K. Improvement of Electrochemical and Thermal Properties of $Li[Ni_{0.8}Co_{0.1}Mn_{0.1}]O_2$ Positive Electrode Materials by Multiple Metal (Al, Mg) Substitution. *Electrochim. Acta* **2009**, *54*, 3851-3856.

(22) Wilcox, J.; Patoux, S.; Doeff, M. Structure and Electrochemistry of $LiNi_{1/3}Co_{1/3-y}M_yMn_{1/3}O_2$ (M = Ti , Al , Fe) Positive Electrode Materials. *J. Eelectrochem. Soc.* **2009**, *156*, A192-A198.

(23) Tang, H.; Zhao, F.; Chang, Z.-r.; Yuan, X.-Z.; Wang, H. Synthesis and Electrochemical Properties of High Density $LiNi_{0.8}Co_{0.2-x}Ti_xO_2$ for Lithium-Ion Batteries. *J. Electrochem. Soc.* **2009**, *156,* A478-A482.

(24) Conry, T. E.; Mehta, A.; Cabana, J.; Doeff, M. M. Structural Underpinnings of the Enhanced Cycling Stability upon Al-Substitution in $LiNi_{0.45}Mn_{0.45}Co_{0.1-y}Al_yO_2$ Positive Electrode Materials for Li-ion Batteries. *Chem. Mater.* **2012**, *24*, 3307-3317.

(25) Schipper, F.; Bouzaglo, H.; Dixit, M.; Erickson, E. M.; Weigel, T.; Talianker, M.; Grinblat, J.; Burstein, L.; Schmidt, M.; Lampert, J. et al. From Surface ZrO_2 Coating to Bulk Zr Doping by High Temperature Annealing of Nickel-Rich Lithiated Oxides and Their Enhanced Electrochemical Performance in Lithium Ion Batteries. *Adv. Energy Mater.* **2018**, *8*, 1701682.

(26) Kim, U.-K.; Myung, S.-T.; Yoon, C. S.; Sun, Y.-K. Extending the Battery Life Using an Al-Doped $Li[Ni_{0.76}Co_{0.09}Mn_{0.15}]O_2$ Cathode with Concentration Gradients for Lithium Ion Batteries. *ACS Energy Lett.* **2017**, *2*, 1848-1854.

(27) Zhou, F.; Zhao, X.; Lu, Z.; Jiang, J.; Dahn, J. R. The Effect of Al Substitution on the Reactivity of Delithiated $LiNi_{(0.5-z)}Mn_{(0.5-z)}A1_{2z}O_2$ with Nonaqueous Electrolyte. *Electrochem. Solid-State Lett.* **2008**, *11*, A115-A157.

(28) Myung, S.-T.; Komaba, S.; Hirosaki, N.; Hosoya, K.; Kumagai, N. Improvement of Structural Integrity and Battery Performance of $LiNi_{0.5}Mn_{0.5}O_2$ by Al and Ti Doping. *J. Power Sources* **2005**, *146*, 645-649.

(29) Araki, K.; Taguchi, N.; Sakaebe, H.; Tatsumi, K.; Ogumi, Z. Electrochemical Properties of $LiNi_{1/3}Co_{1/3}Mn_{1/3}O_2$ Cathode Material Modified by Coating with Al_2O_3 Nanoparticles. *J. Power Sources* **2014**, *269*, 236-243.

(30) Kim, H.-R.; Woo, S.-G.; Kim, J.-H.; Cho, W.; Kim, Y.-J. Capacity Fading Behavior of Ni-Rich Layered Cathode Materials in Li-ion Full Cells. *J. Electroanal. Chem.* **2016**, *782*, 168-173.

(31) Yoon, C. S.; Park, K.-J.; Kim, U.-K.; Kang, K. H.; Ryu, H.-H.; Sun, Y.-K. High-Energy Ni-Rich $Li[Ni_xCo_yMn_{1-x-y}]O_2$ Cathodes via Compositional Partitioning for Next-Generation Electric Vehicles. *Chem. Mater.* **2017**, *29*, 10436-10445.

(32) Ryu, H.-H.; Park, K.-J.; Yoon, C. S.; Sun, Y.-K. Capacity Fading of Ni-Rich $Li[Ni_xCo_yMn_{1-x-y}]O_2$ ($0.6 \le x \le 0.95$) Cathodes for High-Energy-Density Lithium-Ion Batteries: Bulk or Surface Degradation?. *Chem. Mater.* **2018**, *30*, 1155-1163.

(33) Bak, S.-M.; Hu, E.; Zhou, Y.; Yu, X.; Senayake, S. D.; Cho, S.-J.; Kim, K.-B.; Chung, K. Y.; Yang, X.-Q.; Nam, K.-W. Structural Changes and Thermal Stability of Charged $LiNi_xMn_yCo_zO_2$ Cathode Materials Studied by Combined *In Situ* Time-Resolved XRD and Mass Spectroscopy. *ACS Appl. Mater & Inter.* **2014**, *6*, 22594-22601.

(34) Hausbrand, R.; Cherkashinin, G.; Ehrenberg, H.; Gröting, M.; Albe, K.; Hess, C.; Jaegermann. W. Fundamental Degradation Mechanisms of Layered Oxide Li-Ion Battery Cathode Materials: Methodology, Insights and Novel Approaches. *Mater. Sci.& Engineer. B* **2015**, *192*, 3-25.